Understanding phase separation in ZnCdO by a combination of structural and optical analysis

Vishnukanthan Venkatachalapathy, Augustinas Galeckas, Mareike Trunk, Tianchong Zhang, Alexander Azarov, and Andrej Yu. Kuznetsov

Department of Physics/Centre for Materials Science and Nanotechnology, University of Oslo, P.O. Box 1048 Blindern, N-0316 Oslo, Norway

(Received 19 October 2010; published 23 March 2011)

A phenomenon of wurtzite (w), zincblende (zb), and rock-salt (rs) phase separation was investigated in ZnCdO films having Cd contents in the range of 0%–60% settling a discussion on the phase stability issues in ZnCdO. First, low-Cd-content ($\leqslant$17%) ZnCdO was realized preferentially in a w matrix determining optimal Zn-lean conditions by tuning the precursor decomposition rates during synthesis. However, more detailed analysis of x-ray diffraction and photoluminescence (PL) data revealed that the w single-phase stability range is likely to be as narrow as 0%–2% Cd, while samples containing 7%–17% of Cd exhibit a mixture of w and zb phases. Second, high-Cd-content (32%–60%) ZnCdO samples were realized, supplying more of the Cd precursor utilizing Zn-lean growth conditions, however, resulting in a mixture of w, zb, and rs phases. Characteristic PL signatures at 2.54 and 2.31 eV were attributed to zb-ZnCdO and rs-CdO, respectively, while the band gap variation in w-$Zn_{1-x}Cd_xO$ is given by (3.36–0.063x) as determined at 10 K. The phase separation is interpreted in terms of corresponding changes in the charge distribution and reduced stacking fault energy.

DOI: 10.1103/PhysRevB.83.125315 PACS number(s): 64.75.Qr, 81.05.Dz, 78.55.Cr

I. INTRODUCTION

Zinc oxide (ZnO) with a wide band gap (E_g) of ~3.36 eV and a large exciton binding energy of ~60 meV at room temperature is a promising material for optoelectronic application.[1] Moreover, ZnO can be mixed with CdO (E_g ~ 2.3 eV) so that the alloy band gap can be potentially tuned in the range of 3.36–2.3 eV providing additional advantages in device performance. However, ZnO and CdO form in different stable crystal structures—wurtzite (w) and rock salt (rs), respectively—which complicates the fabrication of single-phase alloys in a broad compositional range. Up to now ZnCdO synthesis has been tested by a variety of methods, including metal organic vapor-phase epitaxy (MOVPE),[2,3] molecular beam epitaxy (MBE),[4] and pulsed-laser deposition (PLD),[5] confirming difficulties in maintaining its single phase.

Specific problems most commonly mentioned in literature—coexistence of several phases as well as spontaneous misorientation with increasing Cd content—still remain not fully understood.[3,6] In addition, different groups have reported inconsistent results for E_g and lattice parameters as a function of Cd content.[3–5,7–9]. Concurrently, the solubility of Cd in ZnO prepared by advanced thin-film synthesis was reported to vary in a wide range from 5%[3] to 69% Cd.[7] To the best of our knowledge there is no binary phase diagram for the ZnO-CdO system reported in literature, but several metallurgical experiments with complex oxides have proposed different ranges for solid solubility in the ZnO-CdO system.[10–12] Fundamentally, substituting Zn with Cd in a w-ZnO matrix might result in unfavorable electronic configuration for Cd ions in comparison to that in rs-CdO. However, there are only a few atomic arrangements feasible at a specific ZnCdO composition, limited to the forms of w-ZnO, rs-CdO, and zincblende (zb) matrixes (the latter is known to be metastable for both binary components) or their mixtures. It is also possible that different ZnCdO phases exhibit unexpected—for binary components—stability variations with Zn/Cd content. For example, zb phase, metastable under normal conditions,[13–16] may potentially emerge during a far-from-equilibrium synthesis of ZnCdO alloys, explaining the scattering in literature data. In the present work, we have investigated preferentially (002)-oriented ternary $Zn_{1-x}Cd_xO$ ($0 \leqslant x \leqslant 0.6$) films manufactured by an atmospheric pressure MOVPE and suggest a consistent phase evolution interpretation based on the correlation between x-ray diffraction (XRD) and photoluminescence (PL). The report is structured in the following way. Sec. II contains information on the sample synthesis and measurement details. Sec. III represents the body of the data and is split into subsections. Specifically, Sec. III A explains how the growth-temperature variation was used in order to determine optimal Zn-lean conditions promoting Cd incorporation into ZnCdO. Sec. III B is devoted to the exploration of high-Cd-content ZnCdO, employing various Cd flow rates. Sec. III C deals with the initial calibration of PL features observed in ZnCdO compared to optical signatures of pure w-ZnO and rs-CdO. Reasons and routes for the structural evolution in ZnCdO involving w, zb, and rs phases are discussed in the context of literature data in Sec. IV A. Possible mechanisms for the appearance of mixed w and zb phases are elaborated in Sec. III B accounting for XRD/PL data observed in our samples. Sec. V contains conclusions and is followed by acknowledgements.

II. EXPERIMENTAL

ZnCdO films used in this study were grown on c-axis-oriented sapphire (c-Al_2O_3) by an atmospheric pressure MOVPE. The substrates were cleaned using acetone and ethanol in an ultrasonic bath, followed by cleaning in an H_2SO_4:H_2O_2:H_2O (1:1:6) solution. Prior to inserting into the chamber, the substrates were rinsed with deionized water and dried in N_2 gas. Diethyl zinc (DEZn), dimethyl cadmium (DMCd), and tertiary butanol (t-BuOH) were used as zinc source, cadmium source and oxidizing agent, respectively. The flows of DEZn and t-BuOH were set at 100 and 150 sccm,

respectively. Both DEZn and DMCd bubblers were kept at 10 °C, while *t*-BuOH was maintained at 30 °C. Two methods were employed to vary Cd content in the films: (i) varying the growth temperature while keeping the DMCd flow constant at 20 sccm and (ii) varying the DMCd flow rate and keeping the growth temperature constant at 370 °C. Samples manufactured employing temperature variations were labeled as TX, so that X denotes the actual growth temperature in °C. Samples resulted from flow rate variations were labeled as FX, so that X denotes the actual DMCd flow rate applied in the synthesis in sccm units.

All precursors were carried by N_2 gas and introduced into the chamber through separated injectors, using the so-called "vectored-flow epitaxy" concept, introducing group II and VI precursors separately over a rotating susceptor platen. The rotation of the platen directs the gases across the substrates and out through separate exhausts, avoiding pre-reactions in the gas phase.[17] Effectively, the rotating substrates are alternately "dosed" with certain amounts of group II and VI reagents attached to the surface, and the II/VI precursor ratios in the reaction zone shall depend on the flow rates and decomposition conditions for DEZn/DMCd and *t*-BuOH. In its turn, the decomposition of precursors is governed by the substrate temperature. Thus, exploring the limits of Cd incorporation into w-ZnO, Zn-lean growth conditions[18] found in temperature-variation experiments were applied to maximize Cd content in w-ZnCdO. Further, flow-variation experiments were performed using this optimal Zn-lean condition. The deposition time for all samples was kept at 90 min, resulting in the film thickness in the range of 400–700 nm. Post-deposition anneals, if applied, were carried out in an O_2 atmosphere at 800 °C for 60 min. Pure rs-CdO/w-ZnO samples were also prepared with DMCd/DEZn flows of 150/100 sccm and a *t*-BuOH flow of 150 sccm at 370 °C in order to correlate structural and optical properties with stable binary phases. Note that rs-CdO was synthesized on *r*-axis-oriented sapphire (*r*-Al_2O_3) substrates because only high-index (025) reflections—not attainable by our XRD equipment—are visible in epitaxial rs-CdO/*c*-Al_2O_3 structures.[19]

The crystalline structure of the films was characterized by XRD with Cu K_α radiation (Siemens D5000), specifically revealing epitaxial relationships between the films and the substrates. Indeed, an appearance of a single Bragg reflection detected from the film suggests its epitaxial relationship with the substrate, and full width at half maximum (FWHM) of such a characteristic peak is one of the measures of crystalline quality of the film. For example, w-ZnO grown on *c*-Al_2O_3 is well characterized with its (002) reflection,[20] while (025) and (002) rs-CdO reflections are observed in CdO/*c*-Al_2O_3 and CdO/*r*-Al_2O_3 structures, respectively.[19] Note that XRD features of zb-ZnO appears to be close to those of rs-CdO, with characteristic (002) and (111) peaks at $2\theta = 39.50^\circ$ and 34.00°, respectively.[15–21]

PL properties of the samples were investigated at 10 K and 300 K employing a 325-nm-wavelength cw He-Cd laser with an output power of 10 mW as an excitation source. The emission was collected with a microscope and directed to an imaging spectrometer (HORIBA Jobin Yvon, iHR320) equipped with an electron multiplying charge-coupled device (EMCCD) camera (Andor DL- 658M) and also to fiber-optic spectrometers (Ocean Optics, HR4000 and USB4000) with 0.2- and 2-nm spectral resolutions, respectively. Low-temperature measurements were performed using a closed-cycle He refrigerator (Janis, Inc., CCS450). Normalization of PL signals (if employed) was made to the maximum near-band-edge (NBE) intensity providing a better comparison for PL evolution trends with increasing Cd content.

The chemical composition in the samples was analyzed by Rutherford backscattering spectrometry (RBS) with 2-MeV $^4He^+$ ions backscattered into the detector at 170° relative to the incident beam direction. The stoichiometry of the films was determined from fitting the experimental spectra with simulated curves using the SIMNRA code.[22] Importantly, Cd profiles were found to be flat for all samples and an average content in the plateau was taken as a measure of Cd content in the film. It should be noted that the Cd signal from the higher-Cd-content samples is a non-trivial function of the RBS yield. The complication is due to the generation of a higher amount of secondary electrons from the heavier Cd atoms (comparing to Zn), which affects the dosimetry. Nevertheless, this issue has been taken into account when extracting Cd contents from the RBS spectra.

III. RESULTS

A. Determination of optimal Zn-lean conditions assisting Cd incorporation into ZnCdO

Figure 1 shows typical XRD 2θ scans taken from as-grown ZnCdO films synthesized at various temperatures in the range of 340 °C–430 °C. Note that samples T460, T490, and T520, i.e., grown at 460 °C, 490 °C, and 520 °C, respectively, exhibit XRD patterns identical to that of T430 and are omitted in Fig. 1 for clarity. The angular position of the Bragg peak observed in the T430 film coincides with that of a characteristic (002) reflection in pure w-ZnO within the accuracy of our measurements (see Fig. 1). For the samples grown at lower temperatures, there is a shift toward lower Bragg angles

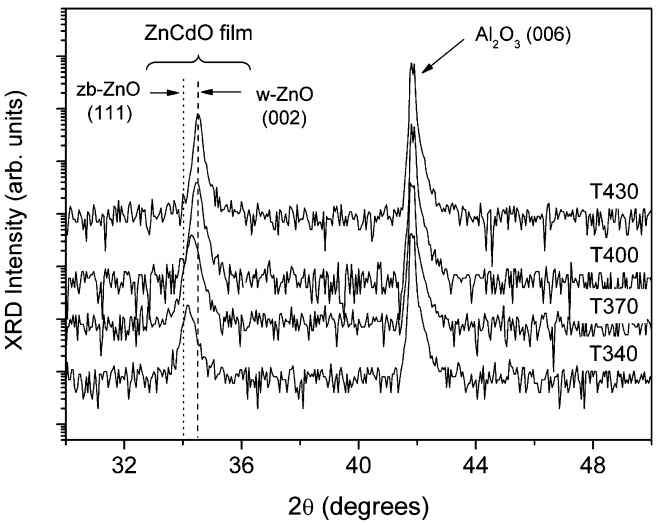

FIG. 1. Typical evolution of XRD intensities in as-grown ZnCdO/*c*-Al_2O_3 structures as a function of growth temperature. The dashed and the dotted lines label (002) and (111) Bragg peaks from pure w- and zb-ZnO, respectively.

(meaning higher interatomic spacing), as observed in Fig. 1, and may be expected from a substitution of smaller Zn atoms (0.74 Å) by larger Cd atoms (0.97 Å)[23] on equivalent crystallographic positions in the wurtzite lattice. Assuming the latter statement is true, there is a clear trend in Fig. 1 showing that the efficiency of Cd incorporation into w-ZnO increases with decreasing growth temperature. No distinct peaks related to reflections from rs-CdO were observed, indicating, in the first approximation, a single-phase wurtzite material in most of the films. However, we cannot exclude contributions coming from zb-ZnO (111) reflections, specifically for sample T340 (see Fig. 1). Indeed, assuming the w matrix is preserved in sample T340, the change in the lattice parameter is (Δc) $\sim$ 0.052 Å, as may be estimated from Fig. 1. However, the corresponding strain ($\sim$1%) is too big to preserve continuous material properties, and the shift in the peak position is likely due to the appearance of (111) zb-related phases. Concurrently, the diffraction pattern in T340 cannot be attributed to pure zb-ZnO only (or zb-ZnCdO) because of a considerable broadness of the peak.

The chemical composition in the films grown at different temperatures was independently analyzed by RBS. Figure 2 shows typical RBS spectra of ZnCdO samples grown at 340 °C, 400 °C, and 430 °C. Positions of O, Zn, and Cd atoms at the film surface are indicated in the figure by arrows. One can see that the fits to the Cd signals (see channels 420–460 in Fig. 2) are quite flat, indicating uniform Cd distribution throughout the film. Note that the RBS yield is proportional to the content of the species, which along with other relevant experimental parameters, were extracted in simulations. The actual Cd content in the samples is shown in the inset in Fig. 2 as a function of growth temperature. Clearly, the growth-temperature variation affects the film composition, showing that Cd content increases up to 17% with decreasing growth temperature from 520 °C to 340 °C.

Figure 3 summarizes the trends for the c-axis lattice parameter and the FWHM of the ZnCdO peak in Fig. 1 as

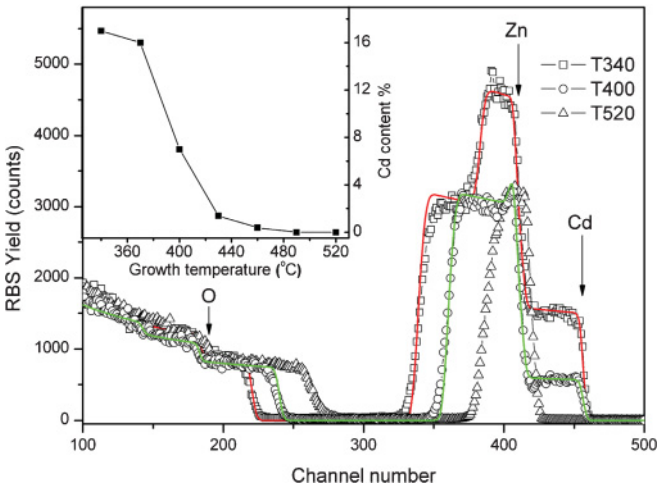

FIG. 2. (Color online) Typical RBS spectra of as-grown ZnCdO manufactured at 340 °C (□), 400 °C (○), and 520 °C (Δ) C, while lines represent the results of fitting. Corresponding Cd content is shown in the inset as a function of the growth temperature for all T-type samples.

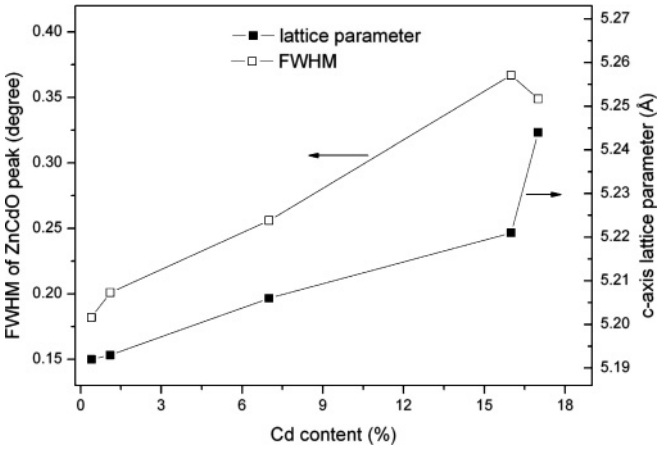

FIG. 3. c-axis lattice parameter and FWHM values extracted from Bragg reflections in ZnCdO films in Fig. 1 as a function of the Cd content.

a function of the Cd content as determined in Fig. 2. It is readily seen from Fig. 3 that the c-axis lattice parameter in ZnCdO films evolves linearly from that of pure w-ZnO (T520) to 5.22 Å (T370) and then increases abruptly for T340. Interestingly, the FWHM values of the (002) diffraction peak also evolve linearly in the same Cd content range (0.4%–16%) and then decreases for the highest Cd content. Considering the Zn-Cd size relationship and taking into account Figs. 1–3, we may assume that the substitution of Zn by Cd takes place on the equivalent crystallographic positions (Zn-sites) in w-ZnO matrix up to Cd content of 16% (T370). It is also likely that the mechanism changes in T340, as is discussed in more detail in Sec. IV, but note already now that the dominating Bragg reflection from T340 is closest to the zb-ZnO (111) position (Fig. 1).

Figure 4 shows the PL spectra obtained from as-grown ZnCdO films synthesized at different temperatures. A strong peak around 369 nm, characteristic of the NBE emission of pure w-ZnO,[1] is observed for samples T490 and T520, in agreement with the results of XRD and RBS analysis in Figs. 1 and 2. With increasing Cd content (see Fig. 2), the NBE emission peak in Fig. 4 shifts toward longer wavelengths and reaches $\sim$494 nm, suggesting $E_g \sim 2.5$ eV for the material grown at 340 °C. Interestingly, as shown in the inset in Fig. 4, already a minor Cd incorporation (0.4% in T460) causes significant shifts of the NBE position with respect to that in pure w-ZnO. Note that with increasing Cd content, the intensity of the NBE emission evolves non-monotonically, combined with a dramatic broadening of the peak (see samples T340–T400). Moreover, distinct shoulders appear at $\sim$450 and 487 nm in samples T340 and T400 on high- and low-energy sides, respectively.

It should be noted that high-Cd-content samples normally exhibit metastable behavior, changing properties dramatically upon post-fabrication annealing. Indeed, an apparent phase separation between w-ZnO and rs-CdO is detected upon annealing in samples T340–T400 by XRD in agreement with the PL observations, resulting in the NBE emission shifts toward $\sim$384 nm irrespective of the initial amount of Cd (indicated as a dashed line in Fig. 4). In its turn, the films

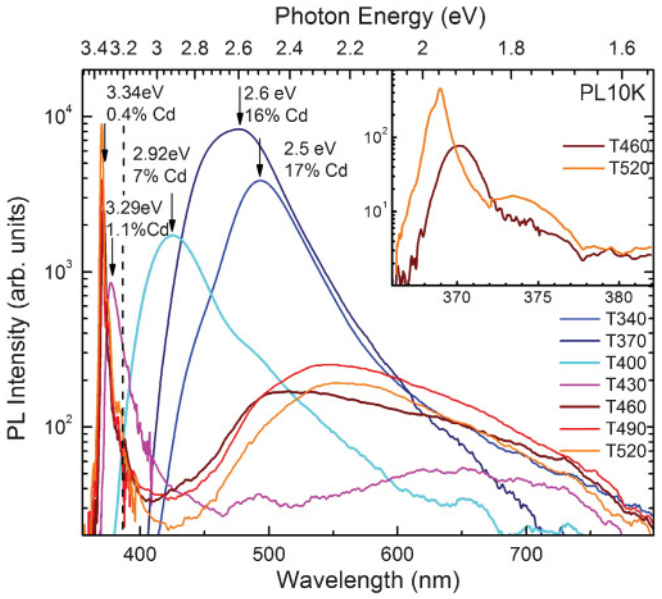

FIG. 4. (Color online) PL spectra taken at 10 K of the ZnCdO films grown at different temperatures. The inset shows the UV-blue part of the spectrum visualizing the manifestation of 0.4% Cd incorporation into ZnO. The dashed line shows a common NBE range where T340–T400 signals shift after annealing. Note that NBE positions in T520–T430 are not affected by post-fabrication anneals.

with low Cd content (e.g., T460 and T430) were found to be stable, i.e., not affected by post-fabrication annealing as confirmed by both XRD and optical measurements, more info in Ref. 24.

To summarize, in spite of the fact that the DMCd flow was maintained constant for the samples in Figs. 1–4, the incorporated amount of Cd is found to vary as a function of the growth temperature, which is also consistent with recent observations by T.Ohashi *et al.*[8] A possible interpretation of the Cd content increasing trend may be done in terms of the precursor decomposition variations as a function of temperature. Indeed, Zn/O lean/rich conditions during MOVPE ZnO synthesis may be readily provided by changing the efficiency of DEZn and *t*-BuOH decomposition solely by tuning the growth temperature.[18] Literally, the pyrolysis of DEZn starts at ∼300 °C and completes at temperatures ⩾385 °C. On the other hand, oxidizing capacity of *t*-BuOH lasts until ∼450 °C. Considering the arguments above, in the context of measurements illustrated in Figs. 1–4, it is likely we have used Zn lean conditions in the low-temperature recipes in our samples. Importantly, DMCd starts to decompose at much lower temperatures, ∼250 °C,[25] meaning that, for example, samples T340 and T370 have been fabricated under Zn-lean conditions, making it possible to incorporate higher Cd content into the films without enhancing DMCd flow rates. The increase in the growth temperature leads to an apparent retardation of Cd incorporation due to the lack of vacant sites, which are instead readily occupied by Zn. Note, however, that increasing of the temperature above 430 °C results in oxygen-lean conditions,[18] and the chemical electronegativity difference between Zn and Cd may limit the incorporation of Cd too. Also, at higher temperatures Cd may desorb from the surface as it is known to be a very volatile element.[26]

B. Exploration of high-content ZnCdO alloys

Optimal synthesis routes—in terms of a combination between Zn-lean conditions and single-line XRD/PL signatures—were determined in Sec. III A, and T370 synthesis was chosen to explore in terms of variation of DMCd flow rates. Figure 5 shows typical XRD 2θ scans taken from the as-grown ZnCdO films fabricated by employing different DMCd flows. The data are labeled in accordance with notations given in Sec. II (note that labels F20 in Fig. 5 and T370 in Fig. 1 represent the same recipe). Similarly to that for T370 in Fig. 1 a single-peak signature is observed for the F20 sample in Fig. 5, indicating within the first approximation a reasonable uniformity in the film. However, new diffraction peaks at $2\theta = 33.3^\circ$ and 38.3° emerge in samples F30–F70 fitting with characteristic rs-CdO (002) and (111) positions, respectively, suggesting a separation between w and rs phases. Interestingly, the position of the wurtzite (002) peak evolves too (compare to a similar evolution in Fig. 1). Specifically, the initial increase in the DMCd flow (e.g., in F30) shifts the reflection (at 34.3° in F20) toward low angles, while the further increase in the flow (samples F40–F70) gradually shifts the peak back to the values characteristic for that in pure w-ZnO (illustrated by a dotted line in Fig. 5). The interpretation for the 2θ changing in the range between w-(002) and zb-(111) positions in Fig. 5 may be similar to that discussed in Sec. III A with respect to possible contributions from corresponding matrixes. Concurrently, the intensity of this peak (follow the dotted line) decreases significantly, along with the FWHM broadening, suggesting that the *c*-axis alignment and crystalline quality in general are strongly reduced with increasing DMCd flow. As a result, the FWHM and the *c*-axis lattice parameter values calculated from the peak positions traced with the dotted line in Fig. 5 evolve in a manner missing a reliable trend. Another prominent shift toward higher 2θ values is also observed for the peak in the range of ∼38.5° in Fig. 5. Again, the magnitude of the shift (see the corresponding dashed line in Fig. 5) is out of range to be explained in terms of a gradual decrease in the lattice parameter in a single phase. However, a combination of Zn incorporation into rs-CdO, Cd incorporation into zb-ZnO, and their intermixing in different magnitudes in different samples may explain this trend in Fig. 5.

The chemical compositions of F-type ZnCdO films were analyzed by RBS and Fig. 6 documents the results of the analysis. The inset in Fig. 6 shows a trend of increasing Cd content as a function of DMCd flow rate. Note that remarkably high Cd content up to ∼60% in F70 was incorporated in our samples, likely assisted by employing Zn-lean conditions. In order to visualize the competition between Cd and Zn atoms, we can replot Cd concentration data as a function of DMCd/DEZn flow ratios as well as to determine the Cd incorporation yield (Y_{Cd}) as a ratio between the actual Cd/Zn content in the film and the DMCd/DEZn ratio in the reactor[9] (see Fig. 7). Note, $Y_{Cd} = 1$ would mean that the stoichiometry of the film is directly proportional to the DMCd/DEZn ratio. For DMCd/DEZn molar ratio ⩾1, Y_{Cd} is only slightly below

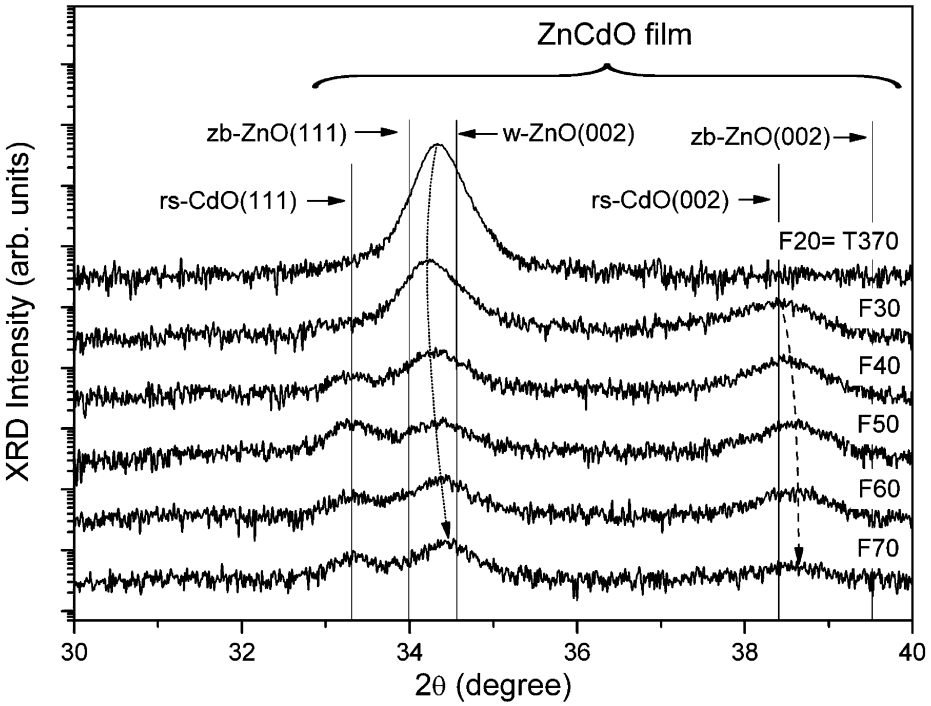

FIG. 5. Evolution of XRD intensities in as-grown ZnCdO films as a function of DMCd flow rate revealing the appearance of different phases. Continuous lines label angles corresponding to the characteristic Bragg reflections from pure w-/zb-ZnO and rs-CdO. Dotted and dashed lines indicate prominent shifts, which are discussed in the text in terms of intermixing of phases characterized by closely positioned peaks.

unity, indeed indicating a better Cd transfer from the gas phase into the films.

Normalized PL spectra taken at 10 K from F-type samples having different Cd contents are depicted in Fig. 8. The spectra are dominated by NBE emission of ZnCdO alloys and exhibit characteristic redshifts consistently with increasing the DMCd flow (meaning increasing Cd content in accordance with Fig. 6). Consistently with XRD (Fig. 5) PL peaks both broaden and decrease in intensity (before normalization—not shown), which implies the deterioration of crystallinity due to the formation of mixed phases. In addition to the dominating NBE emissions, spectral shoulders appear at either lower-energy (samples F30–F50) or higher-energy (samples F60 and F70) sides of the PL peaks in Fig. 8. The spectra were deconvoluted using Gaussian fits and three prominent peaks centered at 487 nm (2.54 eV), 536 nm (2.31 eV), and 590 nm (2.10 eV) were adopted to fit spectra of all F-type samples except for F20, which required an introduction of a higher energy-emission component. Figure 9 shows typical examples of the deconvolution analysis indicating that contributions provided by different components vary with Cd content. Nevertheless, an overall trend in the PL evolution in Fig. 8 is toward domination of the ~536-nm component in the high-Cd-content ZnCdO. Interestingly, the ~487-nm emission used as one of the fitting components in Fig. 9 correlates with the maxima of NBE emissions in samples T340 and T370 as well as with the lower energy shoulder in T400 (Fig. 4), altogether not revealing rs-related diffractions in accordance with Fig. 1. Importantly, the post-fabrication annealing affects F-type

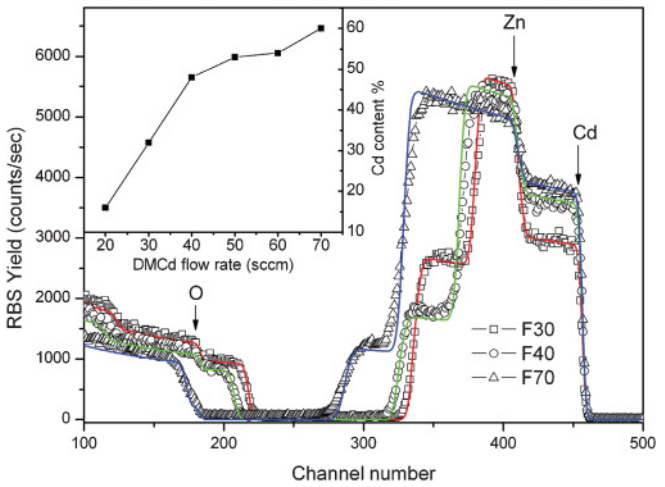

FIG. 6. (Color online) Typical RBS spectra of as-grown ZnCdO synthesized with the DMCd flow rate of 30 (□) , 40 (○), and 70 (Δ) sccm, while lines represent the results of fitting. Corresponding Cd contents are shown in the inset as a function of the DMCd flow rate for all F-type samples.

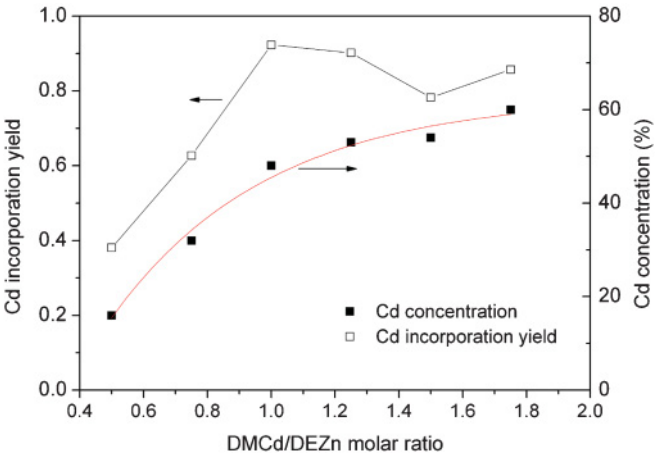

FIG. 7. (Color online) Cd concentration, as determined by RBS and Cd incorporation yield in ZnCdO films as a function of DMCd/DEZn flow ratio in the reactor.

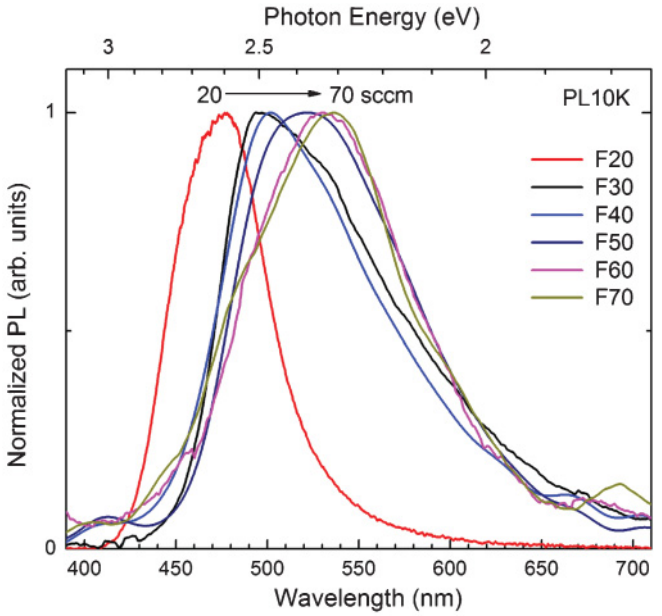

FIG. 8. (Color online) Normalized PL spectra taken at 10 K of samples grown with different DMCd flow rates.

samples in a similar way to that observed in high-Cd-content T-type samples, i.e., after annealing all NBE peaks shift toward ∼384 nm (∼3.21 eV).

C. Calibration of ZnCdO optical signatures with w-ZnO and rs-CdO

Optical properties of pure w-ZnO are relatively well known[1] and, without going into high-resolution measurement beyond our scope, the NBE emission is dominated by excitonic transitions at ∼3.36 eV at low temperature, in agreement with our measurement in samples T520–T490 in Fig. 4. In accordance with literature, rs-CdO exhibits both indirect and direct band gaps at ∼0.84 and ∼2.3 eV, respectively,[27] resulting in a very weak PL due to dominating nonradiative recombination. Nevertheless, Kuo and Huang[28] have observed a PL peak at ∼2.25 eV (550 nm) for CdO nanowires and Xiaochun *et al.*[29] have measured a PL peak at ∼2.33 eV (532 nm) from CdO nanocrystals both to be remarkably close to our 536-nm component in Fig. 9. In order to enhance the comparison, PL from rs-CdO films, manufactured under conditions similar to the rest of the samples, was measured and a typical spectrum is depicted in Fig. 10. In spite of a naturally weak PL signal, we have resolved a dominating peak centered at ∼575 nm in Fig. 10 (2.15 eV[30]), consistent with the literature. Considering Refs. 27–30 along with Fig. 10, we attribute the 536-nm component in Fig. 9 to the NBE signature characteristic of pure rs-CdO. Note that the difference in the peak position (536 nm versus 575 nm) may be explained accounting for Zn contaminating rs-CdO matrix in Fig. 9 as well as elaborated in terms of Burstein-Moss shift due to difference in the strain balance in the films grown on different planes of Al_2O_3.[31] Note that a minor ∼590-nm peak has been observed in both pure rs-CdO[29] and single-phase w-ZnCdO,[2] suggesting this component to involve deeper mid-gap states and/or phonon assisted processes. Importantly, the detection

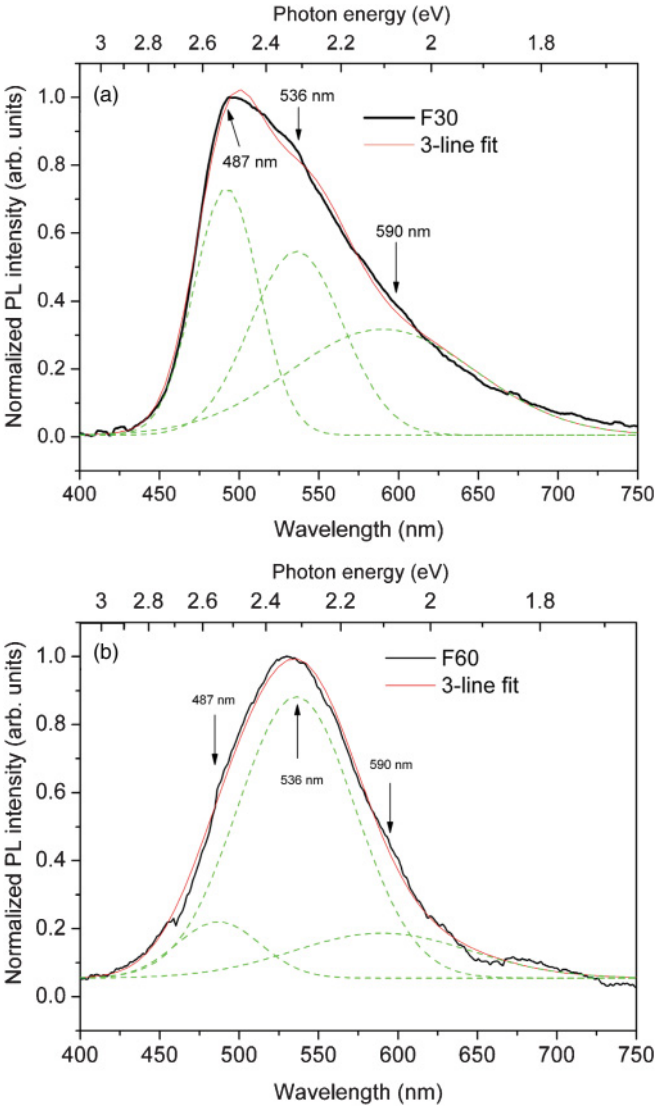

FIG. 9. (Color online) Deconvolution of the normalized PL spectra at 10 K (thick line) for (a) F30 and (b) F60 samples employing a three-line fit. The components used to fit (thin line) the spectra are labeled with arrows.

of the 536-nm component (Figs. 8 and 9) is accompanied with the appearance of rs-CdO-related diffraction signals in Fig. 5 anchoring the calibration. Comparing PL and XRD data implies that the phase separation in the ZnO-CdO system may be a complicated mixture of w and zb and rs phases stabilized at different Zn/Cd contents, which is a matter of a discussion below.

IV. DISCUSSION

A. Reasons and routes for phase separation in ZnCdO

As already mentioned in Sec. I, in spite of a similar elemental chemical character of Zn and Cd, their ternary oxide formation is greatly affected by the appearance of different crystalline structures apparently becoming stable in different compositional ranges. Remarkably, the solid solubility limit of Cd in w-ZnO (S^{Cd}_{ZnO}) is reported to vary between "pessimistic" $\leqslant 5\%$[3] and "optimistic" ∼69%.[7] For

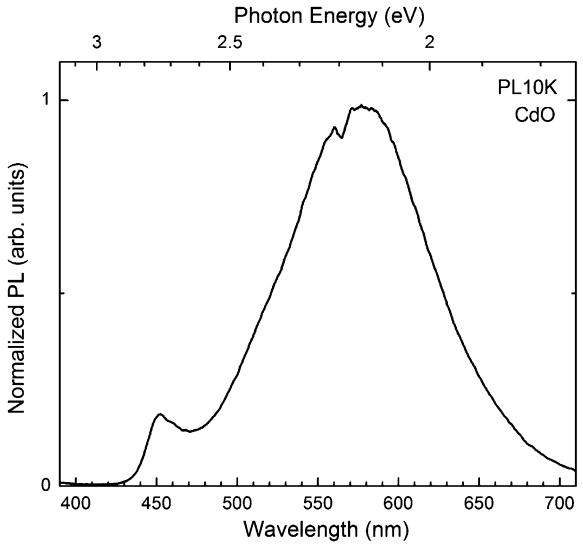

FIG. 10. Normalized PL spectrum of a pure rs-CdO sample grown on *r*-Al2O3 substrate.

example, estimations of low solid solubility of Cd in ZnO may be derived from an early work by Brown and Hummel, who have studied the ZnO-CdO-P_2O_5 system and reported the solubility to be <1% at 800 °C and ∼3% at 1000 °C.[10] Analyzing ZnO-CdO-Fe_2O_3 equilibrium, Bashkirov *et al.* have reported the solubility as high as 12%.[11] More recently, but using similar methodology, Whitaker and Channell studied the ZnO-CdO-B_2O_3 system and found the $S^{Cd}{}_{ZnO}$ value to be negligibly small.[12] The reason for this puzzling variety of solubilities is likely to be that, in spite of Zn/Cd isovalency, ZnO and CdO are not isostructural. Most commonly, Cd when oxidized, adopts octahedral coordination in the cubic B1 rock-salt structure, while ZnO favors tetrahedral coordination in the hexagonal B4 wurtzite structure. Nevertheless, other metastable structures were reported. Specifically, zb-ZnO lies only slightly higher in energy due to its reduced Madelung constant, but the local fourfold coordination is similar to that in the w matrix.[14,32] Interestingly, theoretical calculations by Jaffe *et al.*[33] suggest that a cohesive energy in rs-ZnO (–7.455 eV) is significantly lower than that in w-ZnO (–7.692 eV) while the zb-ZnO has the cohesive energy of –7.679 eV, i.e., very close to that in w-ZnO. Very recently, Zaoui *et al.* have predicted rs-ZnCdO to be more stable than its wurtzite phase for Cd contents >37.5% based on comparison of corresponding cohesive energies[34] (without considering zb structures). Zhu *et al.* have considered all three possible structures—w, zb, and rs—and predicted stabilization of zb-ZnCdO at moderate Cd contents as well as a transition to the rs matrix occurring for Cd content >62%.[13] Though under normal conditions ZnO is thermodynamically stable in terms of its wurtzite phase, zb-ZnO has been fabricated by heteroepitaxy on the zb-like substrates, for example, GaAs.[16] Further, theoretical studies have predicted a difference of ∼80 meV in E_g between w- and zb-ZnO,[35,36] consistent with observations resulting in ∼60-meV difference.[16] Moreover, it has been estimated that the direct band-gap range in zb-ZnCdO is limited to 1.6 eV before the transformation to the rs matrix.[13] Accounting for the similarity in characteristic XRD reflections, the intermixing of w-ZnCdO and zb-ZnCdO may possibly explain the discrepancy in the interpretation of phase equilibria and PL experiments in literature.

At this point, we may conclude that in heteroepitaxial ZnCdO films—metastable by the nature—the actual synthesis may result in different phases stabilized at different growth conditions allowing otherwise nonequilibrium compositions in w, rs, or zb structures to occur (and coexist). For example, considering MOVPE synthesis, the following results are documented in the literature. Ishihara *et al.* has claimed w-ZnCdO single-phase films were synthesized on *a*-Al_2O_3 substrates using remote plasma-enhanced MOVPE with Cd content as high as ∼69%.[7] In a follow-up work from the same group T. Ohashi *et al.* has studied the stability of w-ZnCdO as a function of the growth temperature and detected that critical Cd content for the phase separation decreases from 69% to 50% as the temperature increases from 250 °C to 450 °C.[8] Zúñiga-Pérez *et al.* have reported Cd content of 8.5% in w-ZnCdO fabricated without any phase separation on *r*-Al_2O_3 substrates and claimed 8.5% Cd to be a limit of Cd incorporation into the w-matrix.[9] Gruber *et al.* have reported single-phase w-ZnCdO containing 5% Cd and fabricated on *c*-Al_2O_3 substrates.[3] Interestingly, both Gruber *et al.*[3] and Bertram *et al.*,[6] possibly in the same samples, have observed domains exhibiting lower/high cathode-luminescence (CL) contrasts without deviations in chemical Zn/Cd contents, which may be readily explained by the coexistence of w- and zb-ZnCdO exhibiting a band-gap difference since rs-related reflections likely were not detected. Note that co-existence of the zb and w phases was observed in pure ZnO powder experiments and the phase ratio was found to vary with temperature,[15] which in its turn may explain scattering in $S^{Cd}{}_{ZnO}$ value in literature due to variations in growth conditions. In the next section, we suggest a consistent interpretation of the samples systematically doped with different amounts of Cd as documented in Sec. III.

B. Structural evolution and photoluminescence in the context of responsible mechanisms

Starting with T-type samples, in accordance with Fig. 1 all ZnCdO films are well characterized with reflections within a 34.10°–34.50° 2θ range, and for "zero"-Cd-content samples the peak coincides with that from w-ZnO (002). A gradual increase of Cd incorporation into the w matrix and the corresponding increase in the lattice parameter (see Fig. 3) results in an inevitable accumulation of excess energy (e.g., elastic, electrostatic) that dissipates via segregation in the form of zb-ZnCdO phase[37] minimizing the total energy of the system without macroscopic redistribution of Cd that correlates with a gradual broadening of the diffraction peak (Fig. 3) and dramatic changes in the PL emission in higher-Cd-content samples (Fig. 4). The observed PL peak broadening in T340 and T370 (see Fig. 4) could be due to coexistence of both w- and zb-ZnCdO accounting for, for example, for the zb-/w-band-gap difference of ∼80 meV as detected already in pure ZnO.[35,36] Note, that the PL broadening was observed already in sample T400 containing only 7% Cd, meaning that zb-ZnCdO may form at low Cd contents indistinguishable for XRD (but observed by CL in similar low-content Cd samples[6]). The metastability of T400 is also confirmed by post-fabrication

annealing resulting in the 384-nm NBE shift characteristic for high-Cd-content samples. Further, in accordance with Fig. 5, samples F30–F70 exhibit peaks characteristic for diffraction of w-ZnO and rs-CdO. The appearance of rs-CdO (002) and (111) peaks (not observable in rs-CdO/c-Al_2O_3 structures[19]) may happen due to new epitaxial relationships provided by the w-ZnCdO template in our samples. For example, c/a axes of w-ZnCdO and (002)/(111) directions of rs-CdO match much better compared to a corresponding situation in c-Al_2O_3.

As mentioned earlier, XRD features of zb-ZnO appear to be similar to rs-CdO, with characteristic (002) and (111) peaks but considering their relative contributions to the diffraction pattern in Fig. 5 we may distinguish a clear trend. First, in sample F20 no indication for the (002) zb peak is observed while the contribution of the (111) zb-related signal to the broadening trend in Fig. 5 is evident. The latter may be because zb-ZnO (111) has a better epitaxial relationship with (002) of w-ZnO.[38] With increasing Cd content the rs-CdO (002) signature emerges (F30), broadens, and shifts (F40–F70) toward higher 2θ values while the rs-CdO (111) peak position appearing in F40 remains constant. The shift (see the dashed line in Fig. 5) may be then explained in terms of the contribution from zb-ZnCdO (002). Indeed, with enhancing Cd content and rs-CdO segregation, it is likely that rs-CdO (002) provides a more favorable epitaxial template for zb-ZnCdO (002), explaining also the fact that the diffraction from (111) zb planes weakens (see the dotted line pointing to the w-ZnO peak position in Fig. 5). Importantly, the structural transformation above is consistent with observing different intensities from characteristic emission components, as determined when deconvoluting PL data. To start with, the 536-nm signature is attributed to rs-CdO and its intensity evolves consistently with that of the XRD pattern. The 487-nm feature was found to be dominant in T340, F30, and F40 exhibiting intermediate Cd contents, accompanied with significant contributions from the metastable zb matrix in accordance with XRD shift trends and is tentatively assigned to an excitonic transition in zb-ZnCdO of a certain stable composition. As mentioned above, contributions from the 487-nm feature are detected in all samples having 7% of Cd (see Figs. 4, 8, and 9), indicating that the same stoichiometric Zn/Cd composition in a zb matrix was reached in all these samples. Further, attributing the shifts in the dominating PL signatures in samples having $\leqslant$7% of Cd to the band gap variations in w-$Zn_{1-x}Cd_xO$, a line given by $3.36–0.0627x$ eV fits the data. Note that post-fabrication anneals of samples having 7% of Cd reveal a characteristic 384-nm (3.23 eV) NBE PL signal and a presence of (002) w-ZnCdO and rs-CdO diffractions only allowing to assign the 384-nm emission to a stable w-ZnCdO phase close to equilibrium having $\sim$2% of Cd employing the linear fit above. The latter estimate suggests a solid solubility limit of Cd in w-ZnO of the order of 2%. The interpretations above are illustrated by a schematic in Fig. 11 revealing three characteristic compositional regions.[39] First, alloying w-ZnO with $\leqslant$2% of Cd results in a single-phase w-ZnCdO. Second, for the range of 7%–17% of Cd, w- and zb-ZnCdO phases coexist. Further, samples having 17%–60% of Cd reveal a mixture of w, zb, and rs phases in different proportions. Finally, there could be a narrow concentration range available for the rs-CdZnO single phase stability at very low Zn contents.[40]

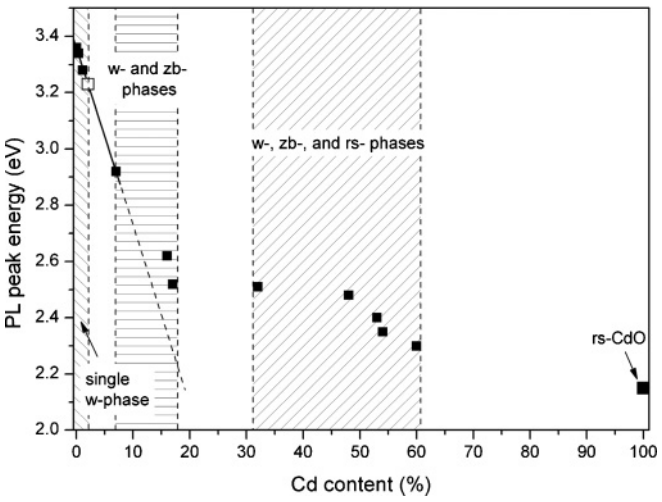

FIG. 11. Dominating NBE PL signatures as a function of Cd content depicted from Figs. 4, 8, and 9 (filled squares) in correlation with corresponding phase stability trends illustrated by dashed lines. The continuous line is a linear fit to the w-ZnCdO-related emissions. An open square represents a characteristic w-ZnCdO signal found after annealing in samples having >7% of Cd.

It should be noted that polytypism, or intermixing of the phases similar to that ascribed in Fig. 11, is also observed in group III–V nanowired zb and w structures, often exhibiting high density of twin planes and stacking faults (SFs).[41] In the bulk form, most of the group III–V materials adopt zb symmetry, while group III nitrides usually exhibit w structure. Nonetheless, there are also reports on GaAs and InP nanowires in the form of w structures,[42,43] as well as on significant w-phase segregation taking place in GaP.[44] Moreover, formation of zb-phase GaN nanowires has been observed, too.[38] Also, the metastable zb-ZnO structures have been stabilized on zb-GaAs(001) substrates by using ZnS buffer layers to minimize the lattice mismatch,[45] whereas w-ZnO has been successfully synthesized on a variety of zb substrates.[46] Several theoretical models address the origin of polytypism in nanowired structures, otherwise exhibiting solely zb or w phases in the bulk, all based on the classic supersaturation concept.[44,47,48] Bearing in mind the arguments above, it is reasonable to anticipate even more prominent and complex polytypism for ternary compounds, such as ZnCdO (see Fig. 11), because of the variety of possible "equilibrium" phases of the two binary constituents before the mixing.

The mechanisms for the structural evolution and PL presented in earlier sections will now be explained in terms of the ionicity of the crystals. Both w-ZnO (zb-) and rs-CdO crystals exhibit electrostatic interaction between the positively charged group II and negatively charged group VI ions. Depending on the Cd content in the ZnO matrix and thus the electronic configuration, different crystal structures become energetically preferable. The stability between sixfold (rs-) and fourfold (w-, zb-) can be predicted considering the ionicity of materials. According to the model proposed by Phillips,[49] the ionicity can be described as $f_i = C^2/(E_h^2 + C^2)$, where

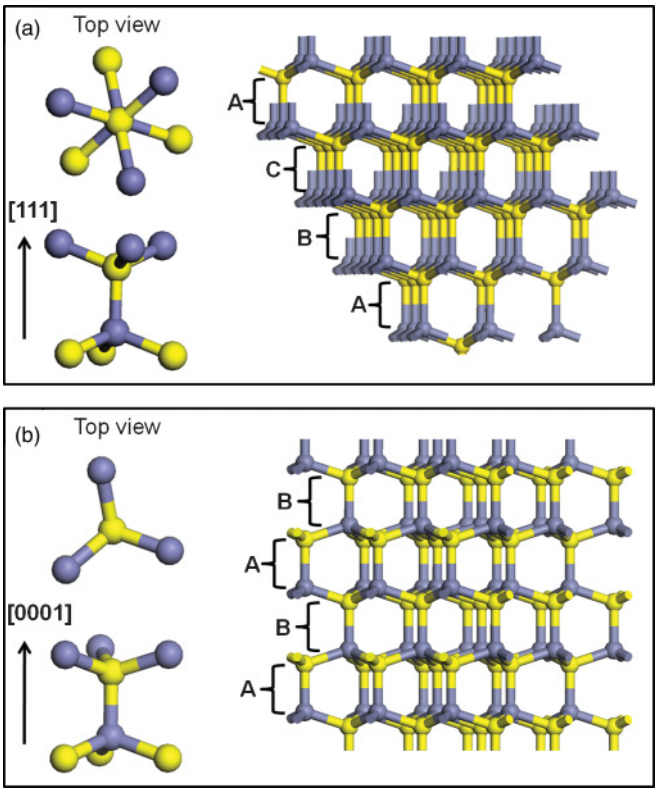

FIG. 12. (Color online) Stacking sequences and zoomed-in views of the bonding configuration in zincblende (a) and wurtzite (b) structures. Different colors denote two sorts of atoms (from group II and VI, respectively).

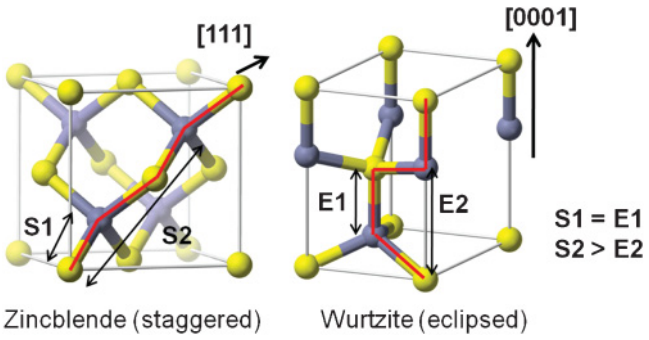

FIG. 13. (Color online) Schematic of (a) staggered and (b) eclipsed configurations, characteristic for zb- and w-structures, respectively, illustrating different distances toward the third-nearest-neighbors (compare S2 and E2).

C and E_h are spectroscopically defined averages of ionic and covalent energy gaps of the pseudopotential in $A^N B^{8-N}$ systems (in our case, $N = 2$ for group II–VI). The competition between closed and open shells, i.e., ionic and covalent bonds, is responsible for the separation of $A^N B^{8-N}$ crystals into sixfold or fourfold coordinated structures. Specifically, group II–VI compounds exhibit a strong ionic behavior with a tendency toward closed-shell configurations, resulting in a sixfold coordinated rs structure. Theory suggests that materials with $f_i < 0.785$ will stabilize in either w or zb structure, while for $f_i \geqslant 0.785$ the rs configuration becomes dominant.[50] These predictions are consistent with the ionicity of 0.616/0.785 and w/rs equilibrium in ZnO/CdO, respectively.[51] In its turn, the instability between w and zb structures can be understood interpreting the increasing interatomic distances and corresponding Coulomb energy with Cd concentration in terms of changes in the stacking fault energy (SFE) and the charge redistribution.[52,53]

In the first approximation, the Madelung constant (α), a parameter describing electrostatic potential of a single ion in a crystal with the ions approximated by point charges, is considered to account for the charge redistribution affecting the w-/zb-phase equilibrium. An ideal w structure with an axial ratio $r = c/a = 1.633$ results in $\alpha_w = 1.6406$,[54] whereas $\alpha_{zb} = 1.6381$ for a zb structure.[55] The changes in axial ratio r will affect the parameter α_w in accordance with $\alpha_w = 1.6406–0.0207\ (r/1.633–1)$[56] (note that for w-ZnO, $r = 1.602$ and $\alpha_{ZnO} = 1.6410$). Assuming that the in-plane lattice parameter a is not affected, the contraction of the lattice in the c direction leads toward higher α_w values, which would stabilize w structure. In contrast, the incorporation of Cd into w-ZnO stretches the lattice in the c direction, hence moving α closer to α_{zb} values. This scenario seems consistent with the evolution of the c parameter shown in Fig. 3 and also with the appearance of the zb-phase signature in Figs. 1 and 4. However, the assumption of constant a may not hold if Cd is incorporated in the w-basal plane. One should also note that atomic units of the zb and w structures exhibit so-called staggered and eclipsed configurations, respectively (see Fig. 12). Indeed, the zb phase exhibits a repeated stacking sequence of three distinct layers of II–VI pairs A-B-C in Fig. 12(a). On the other hand the w-phase is described by a characteristic A-B stacking sequence Fig. 12(b). The energetic difference between these two crystal structures arises from the difference in the third-nearest-neighbor atom spacing, which is shorter for wz than for zb (Fig. 13). The relative energies of these configurations determine the SFE. The change of SFE may be separated into two terms: the bond distortion energy ΔE_b and the Coulomb energy ΔE_c, which correspondingly dominate in low- and high-ionicity crystals. Accounting for a high ionicity (meaning that Coulomb energy dominates), the w structure appears to be more favorable compared to the zb matrix in ZnO because of a shorter distance to the third-nearest(unlike)-neighbor ions in the eclipsed configuration.[56] Similarly to our earlier considerations with regard to α, contraction of the lattice causes ΔE_c to decrease because of the shorter interatomic distances, also meaning the stabilization of the w versus zb structure in ZnO accounting for eclipsed versus staggered stacking. In contrast, a positive strain applied along all crystallographic direction following random Cd incorporation in the Zn-sublattice might result in an increase of ΔE_c enhancing probability of the zb-phase segregation. Takeuchi *et al.*[53] has demonstrated a correlation between the reduced SFE and a process of a charge transfer accompanying the application of strain ε on the bond length, described by $e^* = e_o^*(1 + \varepsilon)^s$, where e^* and e_o^* are the effective charges with and without applied strain, respectively, and s is a charge redistribution index ($s = –3.9$ in ZnO).[53] Thus, a positive strain would decrease the e^* values upon introduction of Cd in w-ZnO, thus contributing to decrease of α and stabilizing zb phase.[57] In w structure, the two-third neighbors

along the *c* axis are much closer than any other similar pairs of neighbors in the w and zb structures,[56] and hence the charge redistribution accompanying the change of *r* may play a decisive role limiting the phase stability. As a result of the gradual strain accumulation in ZnCdO with 7%–17% Cd, the lattice relaxes locally by a mixture of w and zb phases (see Fig. 11). The exact Cd threshold for w toward zb transition is in the range of 2%–7% and remains to be determined via synthesis of new samples applying similar methodology.

V. CONCLUSIONS

The phenomenon of phase separation in ZnCdO was investigated by a combination of structural/optical measurements and the analysis reveals the presence of a new, not conventionally considered, zb-ZnCdO phase in our samples in addition to commonly discussed w and rs phases. First, low-Cd-content ($\leqslant$17%) ZnCdO was realized preferentially in the w matrix determining optimal Zn-lean conditions on behalf of tuning the precursor decomposition rates during synthesis. However, more detailed analysis of diffraction and PL data revealed that the w single-phase stability range is likely to be as narrow as 0%–2% Cd while samples containing 7%–17% of Cd exhibit a mixture of w and zb phases. Second, high-Cd-content (32%–60%) ZnCdO samples were realized supplying more of Cd precursor utilizing Zn-lean growth conditions, however, resulting in a mixture of w, zb, and rs phases. Characteristic PL signatures at 2.54 and 2.31 eV were attributed to zb-ZnCdO and rs-CdO while the band-gap variation in w-$Zn_{1-x}Cd_xO$ is given by (3.36–0.063x) as determined at 10 K. The phase separation is interpreted in terms of corresponding changes in charge distribution and reduced SFE. Interestingly, post-fabrication anneals resulted in stabilization of equilibrium w-ZnCdO phase containing 2% of Cd.

ACKNOWLEDGMENTS

Partial financial support provided by the Research Council of Norway via FRINAT "Understanding ZnO" project and the Nordic Energy Research Agency via N-INNER SolarH2 project are gratefully acknowledged.

[1] U. Ozgur, Y. I. Alivov, C. Liu, A. Teke, M. A. Reshchikov, S. Dogan, V. Avrutin, S.-J. Cho, and H. Morkoc, J. Appl. Phys. **98**, 041301 (2005).
[2] D. W. Ma, Z. Z. Ye, and L. L. Chen, Phys. Status Solidi A **201**, 2929 (2004).
[3] Th. Gruber, C. Kirchner, R. Kling, R. Reuss, A. Wagg, F. Bertram, D. Forster, J. Christen, and M. Schreck, Appl. Phys. Lett. **83**, 3290 (2003).
[4] K. Sakurai, T. Takagi, T. Kubo, D. Kajita, T. Tanabe, H. Takasu, S. Fujita, and S. Fujita, J. Cryst. Growth. **237-239**, 514 (2002).
[5] T. Makino, Y. Segawa, M. Kawasaki, A. Ohtomo, R. Shiroki, K. Tamura, T. Yasuda, and H. Koinuma, Appl. Phys. Lett. **78**, 1237 (2001).
[6] F. Bertram, S. Giemsch, D. Forster, J. Christen, R. Kling, C. Kirchner, and A. Waag, Appl. Phys. Lett. **88**, 061915 (2006).
[7] J. Ishihara, A. Nakamura, S. Shigemori, T. Aoki, and J. Temmyo, Appl. Phys. Lett. **89**, 091914 (2006).
[8] T. Ohashi, K. Yamamoto, A. Nakamura, T. Aoki, and J. Temmyo, Jpn. J. Appl. Phys. **46**, 2516 (2007).
[9] J. Zúñiga-Pérez, V. Muñoz-Sanjosé, M. Lorenz, G. Benndorf, S. Heitsch, D. Spemann, and M. Grundmann, J. Appl. Phys. **99**, 023514 (2006).
[10] J. J. Brown and F. A. Hummel, J. Electron. Soc. **111**, 1052 (1964).
[11] L. A. Bashkirov and N. V. Kornilova, Inorg. Mater. **18**, 1587 (1982).
[12] A. Whitaker and A. D. Channell, J. Mater. Sci. **28**, 2489 (1993).
[13] Y. Z. Zhu, G. D. Chen, H. Ye, A. Walsh, C. Y. Moon, and S-H Wei, Phys. Rev. B **77**, 245209 (2008).
[14] A. Ashrafi and C. Jagadish, J. Appl. Phys. **102**, 071101 (2007).
[15] L. P. Snedeker, A. S. Risbud, O. Masala, J. P. Zhang, and R. Seshadri, Solid State Sci. **7**, 1500 (2005).
[16] A. Ashrafi, Appl. Surf. Sci. **255**, 2342 (2008).
[17] A. J. Clayton, A. A. Khandekar, T. F. Kuech, N. J. Mason, M. F. Robinson, S. Watkins, and Y. Guo, J. Cryst. Growth **298**, 328 (2007).
[18] V. Venkatachalapathy, A. Galeckas, A. Zubiaga, F. Tuomisto, and A. Yu. Kuznetsov, J. Appl. Phys. **108**, 046101 (2010).
[19] J. Zúñiga-Pérez, C. Martínez-Tomás, and V. Muñoz-Sanjosé, Phys. Status Solidi C **2**, 1233 (2005).
[20] J. J. Zhu, T. Aaltonen, V. Venkatachalapathy, A. Galeckas, and A. Yu. Kuznetsov, J. Cryst. Growth **310**, 5020 (2008).
[21] J. Uddin and G. E. Scuseria, Phys. Rev. B **74**, 245115 (2006).
[22] The simulation of RBS spectra was done using SIMNRA code [http://www.rzg.mpg.de/∼mam/].
[23] R. D. Shannon, Acta Cryst. **32**, 751 (1976).
[24] V. Venkatachalapathy, A. Galeckas, R. Sellappan, D. Chakarov, and A. Yu. Kuznetsov, J. Cryst. Growth **315**, 301, (2011).
[25] S. Fujita, S. Matsumoto, and S. Fujita, J. Electron. Mater. **22**, 521 (1993).
[26] V. N. Volodin, V. E. Khrapunov, and R. A. Isakova, Russ. J. Phys. Chem. A **82**, 1075 (2008).
[27] F. P. Koffyberg, Phys. Rev. B **13**, 4470 (1976).
[28] T. J. Kuo and M. H. Huang, J. Phys. Chem. B **110**, 13717 (2006).
[29] W. Xiaochun, W. Rongyao, Z. Bingsuo, W. Li, L. Shaomei, X. Jiren, and H. Wei, J. Mater. Res. **13**, 604 (1998).
[30] Note that the near-band-edge PL emission energy is lower than the actual band-gap energy due to Stokes' shift and the exciton binding energy.
[31] D. Ma, Z. Ye, L. Wang, J. Huang, and B. Zhao, Mater. Lett. **58**, 128 (2003).
[32] C. H. Bates, W. B. White, and R. Roy, Science **137**, 993 (1962).
[33] J. E. Jaffe, J. A. Snyder, Z. Lin, and A. C. Hess, Phys. Rev. B **62**, 1660 (2000).
[34] A. Zaoui, M. Zaoui, S. Kacimi, A. Boukortt, and B. Bouhafs, Mater. Chem. Phys. **120**, 98 (2010).
[35] C. Y. Yeh, S. H. Wei, and A. Zunger, Phys. Rev. B **50**, 2715 (1994).
[36] S. Bloom and I. Ortenburger, Phys. Status Solidi B **58**, 561 (1973).

[37]C. W. Sun, P. Xin, C. Y. Ma, Z. W. Liu, Q. Y. Zhang, Y. Q. Wang, Z. J. Yin, S. Huang, and T. Chen, Appl. Phys. Lett. **89**, 181923 (2006).
[38]B. W. Jacobs, V. M. Ayres, M. A. Crimp, and K. McElroy, Nanotechnology **19**, 405706 (2008).
[39]Note that the windows for appearance of mixed phases in terms of w, zb, and rs structures could vary depending on the deposition techniques/substrates used but, specifically, the Cd solubility limit in w-ZnO should hold irrespective of kinetic routes used in sample manufacturing.
[40]T. C. Zhang, A. Azarov, A. Galeckas, and A. Yu. Kuznetsov (unpublished).
[41]J. Johansson, B. A. Wacaser, K. A. Dick, and W. Seifert, Nanotechnology **17**, S355 (2006).
[42]J. Johansson, L. S. Karlsson, K. A. Dick, J. Bolinsson, B. A. Wacaser, K. Deppert, and L. Samuelson, Cryst. Growth Des. **9**, 766 (2009).
[43]F. Glas, J. C. Harmand, and G. Patriarche, Phys. Rev. Lett. **99**, 146101 (2007).
[44]V. G. Dubrovskii and N. V Sibirev, Phys. Rev. B **77**, 035414 (2008).
[45]A. Ashrafi, A. Ueta, A. Avramescu, H. Kumano, I. Suemuneb, Y-W. Ok, and T-Y. Seong, Appl. Phys. Lett. **76**, 550 (2000).
[46]S. Agouram, J. Z. Perez, and V. Munoz-Sanjose, Appl. Phys. A **88**, 83 (2007).
[47]D. L. Dheeraj, G. Patriarche, H. Zhou, T. B. Hoang, A. F. Moses, S. Grønsberg, A. T. J. Helvoort, B-O. Fimland, and H. Weman, Nano Lett. **8**, 4459 (2008).
[48]M. Moewe, L. C. Chuang, V. G. Dubrovskii, and C. Chang-Hasnain, J. Appl. Phys. **104**, 044313 (2008).
[49]J. C. Phillips, Chem. Phys. Lett. **3**, 286 (1969).
[50]H. Blank, Solid State Commun. **15**, 907 (1974).
[51]C. R. A. Catlow and A. M. Stoneham, J. Phys. C: Solid State Phys. **16**, 4321 (1983).
[52]J. C. Phillips and J. A. Van Vechten, Phys. Rev. Lett. **23**, 1115 (1969).
[53]S. Takeuchi, K. Suzuki, and K. Maeda, Philos. Mag. A **50**, 171 (1984).
[54]F. Keffer and A. M. Portis, J. Chem. Phys. **27**, 675 (1957).
[55]Y. Sakamoto, J. Chem. Phys. **28**, 164 (1958).
[56]P. Lawaetz, Phys. Rev. B **5**, 4039 (1972).
[57]V. S. Urusov, J. Struct. Chem. **9**, 484 (1968).